JOURNAL OF GEOPHYSICAL RESEARCH, VOL. 100, NO. C6, PAGES 10,887–10,904, JUNE 15, 1995

An observational and numerical study of wind stress variations within marginal ice zones

Peter S. Guest
Department of Meteorology, Naval Postgraduate School, Monterey, California

John W. Glendening
Marine Meteorology Division, Naval Research Laboratory, Monterey, California

Kenneth L. Davidson
Department of Meteorology, Naval Postgraduate School, Monterey, California

Abstract. Published studies of ocean mesoscale processes in marginal ice zones (MIZs) using numerical coupled ice-ocean models usually assume that the surface wind speed is constant over the model domain and that wind stress variations are simply proportional to surface roughness variations. We show that this assumption is not realistic in most situations because the surface wind stress is also significantly affected by mesoscale pressure variations, by changes in the surface wind vector, and by changes in surface layer stability. Two numerical case studies, utilizing detailed surface and atmospheric measurements, examine the factors affecting small-scale (<5 km) variations in wind stress within MIZs. These case studies and surveyed observational and modeling results demonstrate that wind stress fields are qualitatively different from the surface roughness fields. A realistic wind stress scenario consists of a maximum just inside the ice edge and another maximum in the open ocean. Stress minima occur within the pack ice region away from the MIZ and over grease ice, if present. The effect of the rougher MIZ ice is counteracted when wind stresses over the open ocean are enhanced by large surface heat fluxes over the ocean, by a strong low level inversion over the ice, or by a sharp atmospheric front with surface winds paralleling the ice edge. Such situations are common in MIZ regions. Some simple methods for including first-order atmospheric effects on wind stress variations, which could be incorporated into current ice-ocean mesoscale models of MIZ regions, are suggested.

Introduction

The transfer of momentum from the atmosphere to the surface (wind stress) is one of the most important air-ice-sea interactions that occurs in high-latitude marine regions. Wind stress transfers momentum directly to sea ice. Wind stress also affects upper ocean currents and turbulence, sea surface tilt, and physical characteristics of the ice pack, all of which are important to ice dynamics. Wind stress can move sea ice over warm water, causing rapid melting and destruction of the pack ice [e.g., *McPhee et al.*, 1987]. Freezing may occur when open water is exposed due to wind-stress-induced divergent ice motion, as in latent heat polynyas. Wind stress can cause formation of leads or ridging and deformation of sea ice. Therefore the validity of any dynamic or thermodynamic sea ice–ocean model depends on the validity of the wind stress field used to force the model.

Air-ice-sea interaction processes are particularly intense in marginal ice zones (MIZs), which are the transition regions between pack ice and open ocean. The concentration, roughness, thickness, floe diameter, temperature, and other characteristics of the sea ice in MIZs are highly variable in space and time. This variability results in complicated air-ice-sea interactions in MIZs.

Paper number 94JC03391.

Several previous modeling studies of sea ice and upper ocean phenomena in MIZs have used wind stress as a crucial input parameter. *Røed and O'Brien* [1983] developed a coupled ice-ocean model which predicted upwelling associated with wind stress variations. *Røed* [1983] used an analytical model to examine upwelling dynamics as a function of stress direction and air-ice, air-water, and ice-water drag coefficient values. *Røed* [1984] developed a thermodynamic model to examine the growth of sea ice in MIZs using constant transfer coefficients. *Smedstad and Røed* [1985] demonstrated that wind stress can cause ice edge banding and other mesoscale ice variations. *Leppäranta and Hibler* [1985] modeled the role of ice interactions in MIZ dynamics. *Häkkinen* [1986a, b] used a coupled ice-ocean model to examine upwelling-downwelling dynamics, eddy generation, and ice banding as a result of a temporally varying wind stress field. *Häkkinen* [1987] included thermodynamics into a dynamical model in order to model ice melting and freezing and entrainment into the ocean mixed layer. *Smith et al.* [1988] examined how sea ice in MIZs interacts with previously existing ocean eddies for cases with and without wind stress. *Kantha and Mellor* [1989a] used a dynamic-thermodynamic multilevel ice-ocean model to model the Bering Sea MIZ and to examine the sensitivity of density structure, ocean circulations, and the ice edge position to changes in various input parameters. *Ikeda*'s [1991] ice-ocean model simulated dipole eddies and mesoscale ice features such as "hammers" and "arches" by subjecting initial ice anomalies to various wind conditions. *Häkkinen et al.* [1992] modeled deep convection forced by strong winds near an ice edge. All these studies assumed that the wind speed and direction at the 10-m elevation were constant throughout the model domain, i.e., throughout the MIZ, so the wind stress magnitude varied only with the surface drag coefficient and the wind stress direction was everywhere the same. One sea-ice model that did include a variable wind forcing was that of *Chu* [1987], but his analytic approach ignored surface roughness changes in the MIZ, so only wind speed variations contributed to the surface stress variations.

In this paper we examine the validity of assuming a constant wind vector when estimating wind stress values in MIZs. First, the surface momentum transfer will be partitioned into five basic factors. The relative importance of these factors will be examined using previously reported and new results from observational and modeling studies of wind stress in MIZs. Some generalizations regarding wind stress in MIZs will be given. Finally, a method for implementing wind stress forcing conditions for use in sea ice and upper ocean models will be provided.

Factors Affecting Wind Stress

The magnitude of the kinematic surface wind stress, τ_{sfc}/ρ, where τ_{sfc} is surface wind stress and ρ is surface air density, can be written as the product of five factors:

$$\tau_{sfc}/\rho = G_{top}^2\,(G_{sfc}/G_{top})^2\,(U_{10}/G_{sfc})^2\,(C_D/C_{DN})\,C_{DN} \qquad (1a)$$

or

$$\tau_{sfc}/\rho = GBWSR \qquad (1b)$$

These factors are (1) factor G, the squared synoptic geostrophic wind G_{top}^2, where G_{top} represents the synoptic-scale or upper level geostrophic wind speed, (2) factor B, a baroclinic factor $(G_{sfc}/G_{top})^2$, where G_{sfc} represents the surface geostrophic wind speed, i.e., the surface pressure gradient, (3) factor W, a wind speed reduction factor $(U_{10}/G_{sfc})^2$, where U_{10} is the wind speed 10 m above the surface, (4) factor S, a surface layer stability factor (C_D/C_{DN}), where C_D is the actual surface drag coefficient and C_{DN} is the neutral surface drag coefficient, both referenced to 10-m elevation, and (5) factor R, a surface roughness factor C_{DN}.

Directional expressions analogous to the magnitude factors G, B, W, and S can also be formed, as indicated by the primes below. (The wind directions here are defined in the downwind sense.) Factor G' is GD_{top}, the upper level or synoptic geostrophic wind direction. Factor B' is $(GD_{sfc} - GD_{top})$, the angular difference between the surface geostrophic wind direction GD_{sfc} and GD_{top}. Factor W' is $(UD_{10} - GD_{sfc})$, the difference between the surface wind vector UD_{10} and GD_{sfc}, also called the "turning angle." Factor S' is $(TD_{sfc} - UD_{10})$, the difference between the surface stress direction TD_{sfc} and UD_{10}, which is nonzero if $\overline{v'w'}$ does not equal 0. The surface stress direction is equal to the sum of factors G', B', W', and S'. For simplicity, discussion and figures in this paper will consider primarily the magnitude of changes in wind stress. However, the reader should be aware that the effects of factors B and W upon wind stress magnitude are associated with corresponding effects of factors B' and W' effects upon the wind stress direction. For example, a large wind speed reduction effect, i.e., a relatively small factor W, is usually associated with a large turning angle, i.e., a relatively large factor W'.

Factor G represents the upper level pressure gradient forcing G_{top}^2. Factor G is the most important factor in (1) because it can vary by orders of magnitude and the corresponding factor G' can be any azimuthal direction. In observational studies, G_{top} is usually defined as the geostrophic wind speed at a level just above surface-induced thermal or dynamic effects. For atmospheric boundary layer (ABL) numerical modeling studies, G_{top} equals the pressure gradient at the top of the model domain; the new and previous numerical studies to be presented in this paper assume that this term is horizontally constant throughout the model domains. The term "geostrophic wind" in this paper refers more precisely to the "gradient wind"; if air parcel trajectory curvature is present, a correction to the geostrophic wind should be applied [e.g., *Holton*, 1972, p. 44].

The strong mesoscale (2–200 km) low level temperature gradients that occur in MIZ atmospheres allow the assumption that mesoscale horizontal pressure variations result primarily from low level temperature gradients and the synoptic-scale (greater than 200 km) pressure variations result from mass distribution in the rest of the atmosphere. Therefore the upper level pressure forcing and the synoptic scale forcing are essentially the same quantity, and the symbol G_{top} will refer to either. Direct measurements of G_{top} require aircraft, rawinsondes, or remote sounders that can measure the wind vector U above the ABL and capping inversion, where winds are quasi-geostrophic. Synoptic-scale pressure fields determined from the existing buoy and land station network can be used to estimate G_{top}, although large errors are possible. However, even when good estimates of G_{top} are available, horizontal wind stress can have considerable variability with respect to the geostrophic wind vector due to factors B, W, S, and R. These factors will be the subject of this study.

Factor B, the baroclinic effect $(G_{sfc}/G_{top})^2$, represents the effect of horizontal thermal gradients in the lower atmosphere on the surface pressure gradient. Pressure variations induced by low level mesoscale structure of the atmosphere are small, O(1 mbar), compared with synoptic variations but can strongly affect the MIZ surface wind because they occur over short distances so gradients are large. The baroclinic factor can be determined from numerical models because the pressure field (or geopotential height) is a prognostic variable. In two-dimensional models the baroclinic factor affects only the along-ice-edge component of the geostrophic wind.

For observational interpretations, the baroclinic factor represents mesoscale pressure variations that cannot be resolved from the routine surface pressure analyses. However, if the mesoscale low level three-dimensional temperature structure can be measured or inferred, then the baroclinic factor can be determined from the thermal wind equation. In the central Arctic, low level mesoscale pressure variations usually are insignificant because surface conditions are generally uniform, although exceptions occur when atmospheric fronts are present. In MIZs, however, strong baroclinic effects are common owing to horizontal changes in ABL temperature and to sloping inversions. This effect is particularly strong if the horizontal temperature variation extends through a deep layer.

Factor W, the wind speed reduction effect $(U_{10}/G_{\mathrm{sfc}})^2$, represents the relation between the surface geostrophic wind speed and the actual surface wind speed U_{10}. A typical central Arctic value for neutral conditions is about 0.4, but this value can vary by a factor of 3 or more across MIZs. Unlike the other factors, this relationship cannot be expressed simply, since it depends upon the terms of the horizontal momentum equation. The wind speed reduction factor is therefore influenced by many significant effects, including surface friction, surface heat flux, thermal wind, advection, and Coriolis turning. It is beyond the scope of this study to analyze all these effects separately. The focus will be on how their net effect changes factor W spatially in MIZs and on its importance relative to other factors.

Factor S, the surface layer stability effect C_D/C_{DN}, represents the effects of virtual temperature flux on wind stress in the surface layer. This relationship is described for horizontally-homogeneous situations by Monin-Obukhov (MO) similarity theory and the Businger-Dyer relationships [e.g., *Stull*, 1988]. Measurements have shown that MO theory can also be used to approximate surface fluxes in some locations where strict horizontal homogeneity is not present, including the MIZ [*Guest and Davidson*, 1991]. Surface layer stability is especially important when surface wind speeds are low and vertical temperature gradients are large.

Factor R, the roughness effect, represented by the neutral drag coefficient C_{DN}, describes the effect of surface roughness on wind stress. The neutral drag coefficient at a reference height of 10 m can be expressed as

$$C_{DN} = \frac{k}{\ln(10/z_0)} \tag{2}$$

where k is von Kármán's constant, assumed equal to 0.4, and z_0 is the roughness parameter. Factor R varies considerably within MIZs. Values range from an average of 0.7×10^{-3} for 100% grease ice coverage to an average of 5.5×10^{-3} for rough, compacted, multiyear ice, with occasional observations outside this range [*Guest and Davidson*, 1991].

We express wind stress in (1) as the product of five factors primarily for illustrative purposes; although four of the factors are composed of dimensionless groups of variables, (1) is not a similarity theory for wind stress because the factors are not all independent. For example, whenever factor R (surface roughness) increases, there will be a counteracting decrease in factor W (wind speed reduction), assuming otherwise constant conditions.

Wind Stress Measurements in MIZs

Background

Previous investigations have studied horizontal wind stress variations in an MIZ, but these have not been evaluated systematically as a group. In this section, wind stress and wind speed measurements taken under a variety of conditions will be compared.

We define a coordinate system relative to a linear ice edge with x representing distance from the ice edge, with negative x used for over-ice locations. Wind direction is defined in the upwind sense so that a relative wind direction of 90° represents on-ice winds (parcels moving at right angles to the ice edge from the open ocean to the ice). A wind direction of 180° represents parallel-left winds (the ice is to left and the open ocean is to the right when looking downwind). Relative wind directions of 270° and 360° represent off-ice and parallel-right winds, respectively.

The product of factors B, W, S, and R equals $\tau_{\mathrm{sfc}}/\rho G_{\mathrm{top}}^2$. This measure of momentum transfer efficiency could be called a "synoptic-scale quadratic geostrophic drag coefficient," or C_g. The average value of C_g for three ranges of x locations and other information obtained from aircraft and modeling studies of wind stress across MIZs are shown in Table 1.

Aircraft Measurements

Aircraft are ideal platforms for quickly obtaining detailed spatial information on atmospheric structure and dynamics. However, since the covariance technique to determine wind stress usually requires averaging over a path length of at least 30 km [e.g., *Walter et al.*, 1984; *Fairall and Markson*, 1987; *Walter and Overland*, 1991], the effect of the smallest MIZ mesoscale features on wind stress cannot be resolved.

Shaw et al. [1991] described the ABL structure and wind stress (covariance method) across an MIZ for a case having parallel-right winds with a small off-ice component. Their aircraft measurements occurred on March 24, 1989, at an elevation of 40–45 m over the Barents Sea MIZ near Bear Island. In general, the wind stress was highest just inside the ice edge and lowest over the pack ice, with intermediate values over the open ocean (Figure 1). There was considerable variation between adjacent points (Figure 1, curve 1). Shaw et al. reported significant baroclinic effects over the ice due to a sloping inversion layer; factor B was equal to 0.17. Over open ocean there was also a sloping inversion, but a horizontal temperature gradient within the ABL counteracted the baroclinic effect at the surface, resulting in a factor B value of 1.00.

Kellner et al. [1987] found that the wind stress in the region just inside the ice edge over was about 40% lower than the open ocean (Table 1 and Figure 1, curve 2), based on an aircraft flight during slightly off-ice winds in the Fram Strait MIZ on July 7, 1984. Although the ABL temperature gradient was small (less than 4°C across the MIZ), there was a change from stable to unstable conditions across the ice edge which apparently had a large influence on wind stress. The lack of a wind stress peak where the ice is probably roughest, i.e., just inside the ice edge, suggests a relatively minor roughness (factor R) effect compared to the combined effects of factors B, W, and S. Kellner et al.'s results were determined by extrapolating wind stress measurements at an elevation of 100 m to the surface; the extrapolation procedure may have caused errors over the ice, since the stable surface conditions could have inhibited mixing within the ABL.

Fairall and Markson [1987] measured turbulence and ABL structure in the Fram Strait on five low level (15-m elevation) aircraft flights during various wind direction regimes in July 1983 using the inertial dissipation method (Table 1 and Figure 1, curves 3–7). The geostrophic winds were not known; therefore only the surface layer wind vector is indicated in Table 1. The light winds, below 6 m s^{-1} for all cases, resulted in quite low wind stress values compared with the other studies (Figure 1). The authors report that in

Table 1. Summary of MIZ Wind Stress Results

Case	Reference	G_{top} (m s^{-1})	GD_{top}[a]	$(\tau_{sfc}/\rho G_{top}^2) \times 1000$ (Mean) $-100 < x < -30$ km	$-30 < x < 0$ km	$x > 0$ km
			Aircraft Measurements			
1	*Shaw et al.* [1991][b]	12.0	345	1.22	1.82	1.37
2	*Kellner et al.* [1987][c]	14.0	345	NA	0.81	1.38
3	*Fairall and Markson* [1987][d]	4.4[e]	350[e]	NA	NA	NA
4	*Fairall and Markson* [1987][f]	3.5[e]	180[e]	NA	NA	NA
5	*Fairall and Markson* [1987][g]	5.8[e]	125[e]	NA	NA	NA
6	*Fairall and Markson* [1987][h]	3.2[e]	130[e]	NA	NA	NA
7	*Fairall and Markson* [1987][i]	4.4[e]	290[e]	NA	NA	NA
			Model Results			
1	*Kantha and Mellor* [1989b][j]	13.0	90	0.89	2.00	1.60
2	*Brown* [1986][k]	10.0	90	0.70	1.85	1.26
3	*Brown* [1986][k]	10.0	270	0.70	2.40	1.26
4	*Kantha and Mellor* [1989b][l]	13.0	270	0.18	1.11	0.87
5	*Bennett and Hunkins* [1986][m]	13.0	270	0.94	0.87	NA
6	*Glendening* [1994][n]	5.0	20	1.38	1.62	0.97
7	*Glendening* [1994][n]	5.0	180	0.49	0.40	0.85

NA, not available.
[a]Relative to ice edge orientation.
[b]Stress measured at 40-m elevation.
[c]Legs V and VI of July 7, 1984, flight. G_{top} and GD_{top} based on upper level winds from rawinsonde soundings.
[d]Flight 2, July 15, 1983.
[e]G_{top} was not available, so 15-m wind speed and direction are shown instead.
[f]Flight 4, July 25, 1983.
[g]Flight 6, July 27, 1983.
[h]Flight 8, July 29, 1983.
[i]Flight 9, July 30, 1983.
[j]The most realistic case (case 3) is shown. This same case was also simulated by *Overland et al.* [1983], *Reynolds* [1984], and *Wefelmeier and Etling* [1991]. The latter three studies gave results similar to those of *Kantha and Mellor* [1989b] and are not shown.
[k]Includes the speculated changes from equilibrium values shown in Figure 21 of *Brown* [1986].
[l]Based on their case 3 on-ice wind simulation.
[m]Based on their "rough" ice case.
[n]Based on a 40-km transition region in surface roughness.

general, the surface layer stability effects (factor S) were the same order of magnitude as the surface roughness effects (factor R) and that the baroclinic effects produced changes that were as large as 6 m s^{-1}, a magnitude comparable to the surface winds. Both the *Fairall and Markson* [1987] and the *Kellner et al.* [1987] studies showed that effects of stability and baroclinic and ABL structure on wind stress can be substantial during the summer, despite modest horizontal surface temperature gradients (less than 5°C across the MIZ).

Surface Platform Measurements

Buoy and ship measurements cannot provide the spatial resolution of aircraft measurements, and direct stress measurements are difficult. For these reasons we cannot show high-resolution wind stress variations such as in Figure 1. However, surface platforms do provide relatively long time series of wind speed values that can be used to analyze variations across MIZs.

During the Marginal Ice Zone Experiment (MIZEX) and Coordinated Eastern Arctic Experiment (CEAREX), hundreds of surface wind measurements were performed by the authors and associates from several ship and ice floe platforms in various locations and seasons within the MIZ region of the East Greenland Sea and Fram Strait regions. By calculating the median wind speed in 50-km bins of distance from the ice edge, a composite cross section of wind speed in the MIZ is constructed (Figure 2). Smaller-scale binning is not justified because of uncertainties in exact ice edge location, defined here as the 50% concentration isopleth, and differences in ice conditions between observations. There is a significant trend of increasing wind speed from the ice region to the open ocean when all data are considered, although there are some statistically significant differences between different seasons and wind direction regimes. The nonsummer, on-ice wind category has the largest difference in median wind speed across the MIZ (a factor of 2.5); this category is most favorable for the formation of a shallow internal ABL over the ice with consequent reduction in wind speed. The composite wind speed variations across the MIZ represent changes in wind stress by factors ranging from 2 to 12, which are comparable to or greater than those due to surface roughness variations.

During a 3-day period, off-ice surface winds were measured with ship, buoy, and ice tower platforms along a 190-km line across an ice edge in the Bering Sea during March 1981 [*Lindsay and Comiskey*, 1982; *Reynolds*, 1984]. The wind speed was 10–350% higher over the open ocean (x = 100 km) than over the ice (x = −90); the average increase was 20%.

Andreas et al. [1984] describe measurements from a ship transect across the Antarctic MIZ in October 1981 during on-ice wind conditions. The wind speed increased from 8 m s^{-1} to 10 m s^{-1} from an ice-covered to an open-ocean region 150 km upwind.

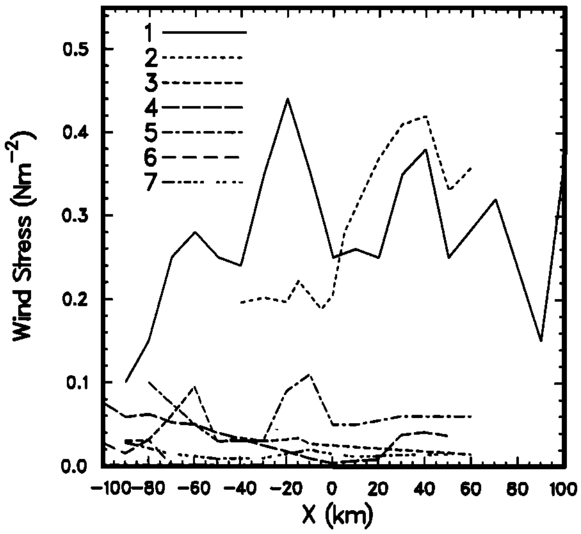

Figure 1. MIZ surface wind stress as a function of distance from ice edge, based on aircraft measurements. The ice edge ($x = 0$) is defined as the 5% ice concentration isopleth. The line numbers represent the seven cases listed in the top section of Table 1.

Guest et al. [1995] describe a 6-day period of remarkably constant parallel-right winds in the Fram Strait MIZ during March 1989. Several ship transects with rawinsonde profiles revealed a large contrast in conditions across the ice edge with a 200-m-thick, −20°C ABL over the ice and a 1000-m-thick, −4°C ABL over the open ocean. The average wind speed varied from 4 m s^{-1} to 12 m s^{-1} between $x = -30$ km and $x = 30$ km, indicating that factor W changed by a factor of 9 across the ice edge region.

The observations cited in this section provide quantitative observational evidence that significant systematic variations in wind speed exist in MIZ regions. With the exception of some of *Fairall and Markson*'s [1987] light wind cases, the average wind speed over ice-covered regions was lower than that over open ocean regions.

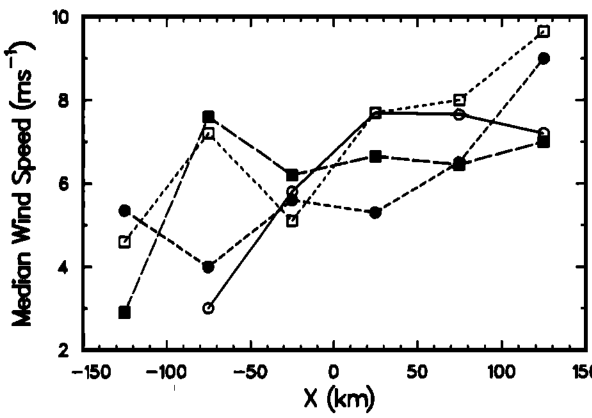

Figure 2. Median wind speed as a function of distance x from the ice edge, for the East Greenland Sea and Fram Strait MIZ using data collected by the authors. The symbols represent these different cases: off-ice wind, summer (solid squares), on-ice wind, summer (solid circles), off-ice wind, nonsummer (open squares) and on-ice wind, nonsummer (open circles). There are no data available for the on-ice, nonsummer category in the bin centered at −125 km. The average standard deviation within each distance bin for each category is 4.7 m s^{-1}, and the average standard error is 0.8 m s^{-1}.

Models of Wind Stress in MIZs

Numerical models of the ABL enable one to make controlled studies of wind stress variations in MIZ regions. Before some new modeling results are presented in the next section, some previous studies will be briefly summarized (Table 1, bottom section).

Overland et al. [1983], *Reynolds* [1984], *Kantha and Mellor* [1989b], and *Wefelmeier and Etling* [1991] modeled off-ice wind cases using the *Lindsay and Comiskey* [1982] observations for initialization and boundary conditions. Virtually the same results were obtained by these studies; here we present the *Kantha and Mellor* [1989b] results (Figure 3, curve 1). A C_D of 3.8×10^{-3} was used for a rough ice region, -30 km $< x < 0$ km, while a C_D of 2.0×10^{-3} was used elsewhere. The highest wind stress values occurred in the rough ice region, with the lowest values occurring over the pack ice and moderate values over the open ocean. *Brown* [1986] modeled an ice edge representative of the Bering Sea during off-ice winds and obtained a similar wind stress pattern (Table 1 and Figure 3, curve 2).

Brown [1986] and *Kantha and Mellor* [1989b] also modeled on-ice wind cases (Table 1 and Figure 3, curves 3 and 4, respectively). Again, both studies found that the highest wind stress occurred just inside the ice edge, the lowest values occurred over the pack ice, and intermediate values over the open ocean. The *Kantha and Mellor* [1989b] simulation produced a very stable and shallow ABL over the ice which greatly reduced the wind speed and wind stress (Table 1). *Bennett and Hunkins* [1986] modeled the on-ice wind case described by *Andreas et al.* [1984] (see above). Unlike the previous cases, the characteristics of the ABL were only slightly modified across the MIZ; therefore surface roughness variations (factor R) were more important to the wind

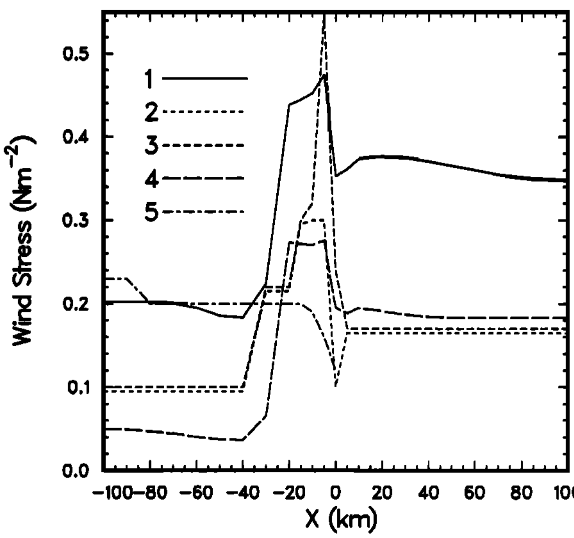

Figure 3. MIZ surface wind stress as a function of distance from ice edge for the first five modeling studies listed in the bottom section of Table 1.

stress variations than the wind speed variation (factor *W*). Wind stress increased sharply at the ice edge and did not decrease deep within the MIZ like the other model studies.

The most dramatic variability in ABL structure and associated wind stress effects occurs during periods when surface winds are parallel to the ice edge. Surface thermal fronts and discontinuities in ABL depth often occur during parallel wind situations. These features are associated with large variations in wind speed and direction over small horizontal distances. *Glendening* [1994] modeled the effect of wind direction relative to an ice edge. Across the ice edge, from ice to open ocean, his surface temperature increased by 4°C, and factor *R* (surface roughness) decreased by a factor of 3. Strong ABL frontal structures, with large vertical velocities, occurred near the ice edge for relative geostrophic wind directions near 25° and near 175°, the latter being slightly weaker. The frontal characteristics were sensitive to small changes in the wind direction for these near-parallel wind cases. For other wind directions the frontal features were advected away from the edge, and sharp thermal gradients could not be maintained at the ice edge. *Kantha and Mellor*'s [1989b] numerical model also produced a sharp surface front for winds nearly parallel to the ice edge.

Glendening [1994] analyzed MIZ variations of similar surface stress factors for two sharp frontal cases, having oppositely directed geostrophic winds with surface winds nearly paralleling the ice edge (Table 1). The weak geostrophic forcing (G_{top} = 5 m s^{-1}) created wind stress magnitudes that were too low to show in Figure 3. Overall, the effects on wind stress of surface wind speed variations (product of factors *B* and *W*) was comparable to the surface roughness effect (factor *R*). For parallel-right surface winds the wind speed variations more than counteracted the change in roughness near the ice edge. For parallel-left winds the wind speed had three maximums, one near the ice edge, one over the pack ice, and another in the open ocean. This produced wind stress curl reversals near the edge and approximately equal wind stress over the interior pack ice and open ocean regions. Variations of the surface stability effect (factor *S*) were comparable to those of the roughness factor for parallel-right winds but were relatively minor for parallel-left winds.

Such frontal structures are especially important to wind stress variations for two general reasons. First, the baroclinic effect (factor *B*) is strongest within a frontal region with large temperature gradients. The effect can either decrease or increase the surface wind depending on the orientation between the vertically integrated thermal gradient vector and the geostrophic wind vector. Second, the surface front is often the transition region between the relatively low wind speed regime associated with shallow central Arctic ABLs and the relatively high wind speed regime associated with deep marine ABLs. This difference, resulting from the low level inversion over the pack ice, gives a large speed reduction effect (factor *W*).

Case Study Modeling

Background

Mesoscale (2–200 km) variations in factors B, W, S, and R and the resulting wind stress fields will be analyzed in detail for two case studies by incorporating surface and upper level meteorological measurements into a two-dimensional numerical model of the MIZ ABL. Although each case study represents a unique situation, many of the results will be applicable to understanding MIZ wind stress variations in general.

These case studies differ from previously published MIZ ABL studies in that they are designed specifically to analyze the relative effect of factors B, W, S, and R on wind stress. This study also includes a more detailed treatment of surface forcing conditions (temperature and roughness) than did previous studies.

Resolution of the small-scale variations in atmospheric forcing input into ice-ocean models is important because wind stress variations at these small scales may generate mesoscale ocean features. For example, *Johannessen et al.* [1985] report values of the internal Rossby deformation radii of the upper ocean of 3–5 km and ocean eddy radii of 5–15 km in the Fram Strait MIZ; these values are smaller than those for most other ocean regions.

ABL Model Description

The two-dimensional hydrostatic model uses a turbulent kinetic energy (TKE) equation to predict turbulence and mixing and employs a finite-element technique to better resolve ABL gradients. MO similarity scaling is employed for the surface layer. The horizontal resolution varies from 3 km near the ice edge to several tens of kilometers near the lateral boundaries. The model does not contain moisture, cloud physics, or radiation physics, but radiation effects on the surface temperature are included in the surface boundary condition formulation. The model is run for a 24-hour simulation, by which time a quasi-steady state is reached. For details on the ABL model, see *Glendening* [1994].

Surface Model Description

Surface roughness. Surface roughness and heat flux are crucial parameters that need to be accurately specified to produce realistic wind stress fields in MIZs. The key parameters for determining the surface fluxes of momentum and heat are wind speed U_{10}, air temperature T_{air}, roughness length z_0, temperature roughness length z_{0t}, and surface temperature, T_{sfc}. The ABL model provides the value of U_{10} and T_{air} at a reference level (10 m) within the surface layer. The surface temperature T_{sfc} is defined as the temperature at the atmosphere-ice or atmosphere-water interface. The methods for determining the three parameters z_0, z_{0t}, and T_{sfc} are now described.

The surface roughness is determined by first identifying the types and concentrations of ice present in a grid point area and then determining the roughness corresponding to those ice conditions. Synthetic aperture radar (SAR) provides high-resolution images of radar backscatter which can be used to identify ice type.

For the first case study, ice types were classified based on mosaics of SAR images produced by R. Shuchman and associates at the Environmental Research Institute of Michigan as part of the 1987 Marginal Ice Zone MIZ Experiment (MIZEX-87). The authors gained experience at identifying ice types from the SAR images by comparing the SAR images of the area around research ships with the ice characteristics as observed from the ships for several different periods during MIZEX-87 and other Arctic programs. Once the ice type had been classified, it was assigned a z_0

value based on *Guest and Davidson*'s [1991] results of ice type versus z_0.

Surface heat flux. The surface heat flux parameterization depends upon the temperature roughness scale z_{0t}, and the surface temperature T_{sfc}. The method suggested by *Andreas* [1987] is used to determine the temperature roughness scale, z_{0t}, based on the value of z_0 and a roughness Reynolds number. The turbulent heat flux calculations assume that the temperature at z_{0t} m above the surface interface is equal to the surface temperature T_{sfc}.

The numerical ABL studies models previously discussed either fixed T_{sfc} or assumed heat flux over ice to be zero. To determine the sensible heat flux more realistically over sea ice, T_{sfc} is determined at each time step by using a linearized analytical formula that includes the effects of atmospheric radiational, turbulent heat fluxes, and conductive heat flux through the ice [*Guest and Davidson*, 1992], similar to the methods used by *Parkinson and Washington* [1979] and *Maykut* [1982]. Over the open ocean, T_{sfc} is specified based on observations and does not change with time.

Case Study 1: ABL Front Near Ice Edge

Measurements

The first case study demonstrates the effects of an atmospheric ice edge front on the wind stress vector. The model simulates conditions on April 1, 1987 (all times are UT), in the Fram Strait MIZ during the MIZEX-87 project (Figure 4). The R/V *Polar Circle* and R/V *Haakon Mosby* are located inside and outside, respectively, a compact ice edge which is approximately linear for 200 km upwind. (For the case studies the ice edge is defined as the 50% ice concentration isopleth.) Standard surface and upper air meteorological

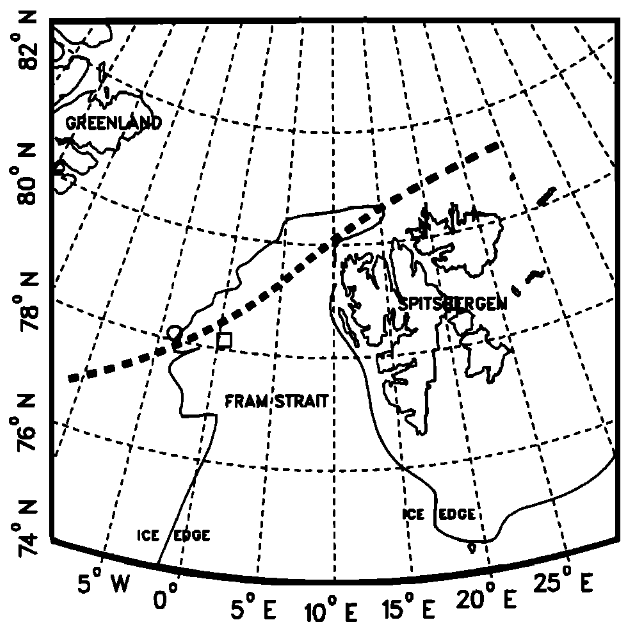

Figure 4. Map of case study 1 simulation showing location of R/V *Polar Circle* (circle), R/V *Haakon Mosby* (square) and ice edge (solid line) for 1800 April 1, 1987. The thick dashed line represents an air parcel trajectory above the boundary layer (ENE to WSW downwind). The model domain represents a section at right angles to the ice edge in the region between 78°N and 80°N.

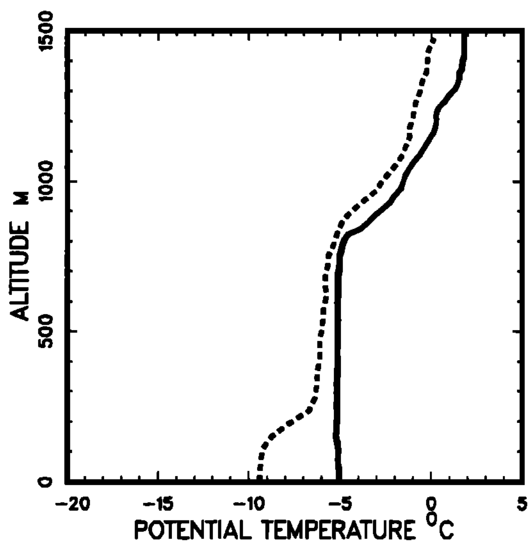

Figure 5. Profiles of potential temperature for the R/V *Polar Circle* (dashed line) and R/V *Haakon Mosby* (solid line) at 1655 and 1745 UT, respectively, on April 1, 1987. Locations are shown in Figure 4.

measurements, surface radiation measurements, wind stress measurements, surface characteristics observations, and cloud observations were taken on both ships. The wind at the *Polar Circle* location is backed approximately 40° from the *Haakon Mosby* winds. Mesoscale pressure fields cannot be determined directly, but the analyzed synoptic geostrophic wind is from an ENE direction, or 35° relative. Similar winds above the ABL at both ships (not shown) support the evident lack of strong variations in the background pressure gradient.

The air in the lower 2 km of the atmosphere in the vicinity of the ships was originally part of a cold Arctic air mass located north and east of Svalbard. As the air moves over the open ocean west of Svalbard, large surface heat fluxes deepen the mixed layer to 825 m at the *Haakon Mosby* (Figure 5). The mixed layer is relatively cold at −5.0°C, compared with the warm surface temperature of −1.7°C, indicating that the ABL is unstable and still deepening at the *Haakon Mosby*. The potential temperature profile at the *Polar Circle* location is nearly identical to that at the *Haakon Mosby*, except for a 200-m-deep cold layer at the surface, created by contact with the ice. Above the shallow ABL over the ice, and everywhere over the ocean, the wind direction is 35° relative, indicating an on-ice component. But in the cold over-ice ABL layer, the wind direction is 340° relative, indicating a small off-ice component. These conditions persist from 0000 to 1800 on April 1, approximating a steady state condition.

The entire region is covered by a low stratocumulus deck capped by the marine inversion, i.e., the upper inversion over the ice. Some broken midlevel (2000–5000 m) cloud layers are present at the *Haakon Mosby* location.

Wind stress at the ships was periodically measured on April 1 with hot film anemometers using the turbulent kinetic energy method [*Guest and Davidson*, 1987, 1991]. Wind stress measurements at the *Polar Circle* indicate that the average value of the 10-m neutral drag coefficient C_{DN}, is 4.2 $\times$ 10^{-3}. At the *Haakon Mosby* the average neutral drag

Table 2. Surface Conditions for Case Study 1

Surface Type	x, km	$C_{DN} \times 1000$
Pack ice	<-100	2.2
Inner MIZ	-100 to -12	2.2–4.0
Compact outer MIZ	-12 to -1	4.1–4.3
Compact brash/rubble	-1 to 0	5.6
Ice edge	0	
Grease/pancakes	0 to 10	1.4–0.9
Open/grease	10 to 160	0.8–1.8
Open	>160	1.8

coefficient is 0.9×10^{-3}, considerably less than a typical open ocean value of 1.2×10^{-3} [*Smith*, 1988] or a Greenland Sea ice-free value of 1.8×10^{-3} [*Guest and Davidson*, 1991]. This low C_{DN} is due to the presence of grease ice, which reduces surface aerodynamic roughness by damping capillary and gravity waves. This grease ice effect was measured several times during MIZEX-87. During the case study period, winds on April 1 and previous days had moved the ice edge to the northwest, toward the ice interior. The ice movement left behind surface water with a temperature of $-1.7°$C, extending about 100 km from the 1700 April 1 ice edge location. When exposed to the Arctic air mass and moderate wind speeds, this cold water formed grease ice with a surface area coverage of greater than 80% from the *Haakon Mosby* to the ice edge. The effects of grease ice are included in our case study simulation.

Model Initialization and Boundary Conditions

Domain. The model represents a vertical slice perpendicular to the ice edge (xz plane). An upper level geostrophic wind G_{top} of 9 m s^{-1} is assumed at all grid points with a direction of 35° relative. The initial temperature profile above 1000 m is set to the *Haakon Mosby* values. Below 1000 m the initial potential temperature linearly decreases to $-19.1°$C at the surface, representing the Arctic air mass located north of Svalbard. The model domain, from left to right, includes a 205-km region of pack ice and MIZ representing the ice region east of Greenland, a 230-km stretch of open water representing the ice-free region west of Svalbard, and a 130-km ice region on the right representing the ice area north of Svalbard (Figure 4). The model surface conditions are based on conditions along the upwind trajectory shown in Figure 4, rather than exactly perpendicular to the ice edge. The right side ice edge and ice region are included in the domain to produce the unstable surface conditions observed at the *Haakon Mosby* location. Because the area where x is greater than 230 km is not part of the area of interest, it will not be discussed further.

Ice conditions. Ice types and concentrations are estimated from the SAR images and ship observations along a transect perpendicular to the ice edge, which is defined as the 50% ice concentration isopleth. The different surface regions and their C_{DN} values are summarized in Table 2 and Figure 6. A wide inner MIZ represents the transition between undeformed pack ice and a relatively narrow outer MIZ representing swell-affected broken floes. The large roughness created by a thin strip of rubble along the compact ice edge contrasts greatly with the adjacent open ocean damped by grease ice. Farther off-ice, grease ice concentrations gradually decrease so the roughness increases to open ocean values.

Surface temperature. The surface temperature T_{sfc} is a predicted variable, based upon a surface energy balance. Our method requires specification of downward longwave radiation, net shortwave radiation, turbulent fluxes, an effective conductivity, and an internal ice temperature. The ice is compacted within the ice edge, so little heat comes from leads. The downward longwave radiation Q_{LDOWN} measured at the *Polar Circle* location is 259 W m^{-2}. The average net shortwave radiation Q_{SNET} measured is 7 W m^{-2}. Farther into the ice the cloud bottoms are colder, and Q_{LDOWN} is estimated to be 253 W m^{-2}. The snow and ice densities, thicknesses, and salinity required to estimate conductive heat flux are based on a few direct measurements by scientists aboard the *Polar Circle* and observations from the bridge. An important factor is the presence of a 2-cm layer of insulating dry new snow in the MIZ. Based on a time period of 24 hours and the thermal diffusivity of the snow-ice surface, an effective depth d_{eff} is defined for each x location [*Guest and Davidson*, 1992]. The effective depth represents the deepest location within the snow or ice which has a thermal influence on the surface. For snow or ice thinner than d_{eff} the surface is influenced by the ocean temperature of $-1.7°$C. For thicker snow or ice the temperature at d_{eff} is specified as calculated from a multilevel snow-ice thermodynamic model [*Guest*, 1992]. The resulting surface temperature field (Figure 6) is dominated by radiation over the interior ice and most of the MIZ. Only within 3 km of the edge, where new snow is moist or washed away, does conduction become more important than radiation in determining surface temperature. Note that in the region between $x = -15$ km and $x = -5$ the surface temperature is relatively low while the roughness is relatively high (Figure 6). This will be shown to have important implications for the resulting wind stress field. In the grease ice and open ocean regions, surface temperature is $-1.7°$C, constant with time. The sensible heat flux was small and downward over the ice and moderately upward over the open ocean (Figure 6).

Results

Temperature structure. The model produces an inversion based at a height of approximately 1000 m over the open ocean with a low level inversion creating a shallow ABL

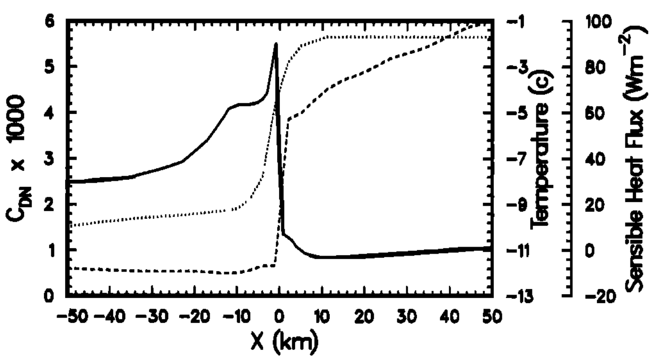

Figure 6. Surface boundary conditions for case study 1. The average surface temperature (dotted line) and heat flux (dashed line) at the end of the model run and the neutral drag coefficient C_{DN} (solid line) throughout the run are shown as a function of distance from the ice edge, x.

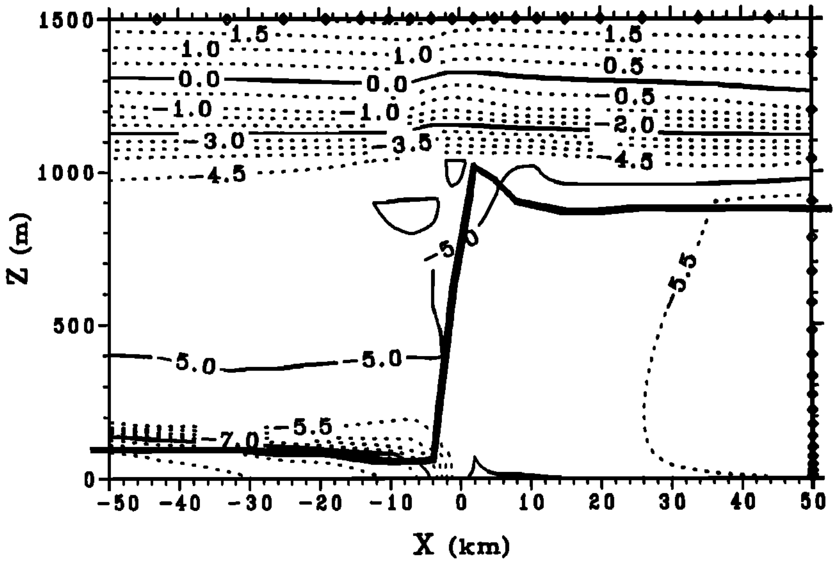

Figure 7. Isotherms of potential air temperature generated by the model simulation for case study 1 in increments of 0.5°C, with every fifth isotherm solid. The solid thick line represents the top of the ABL, defined as the location where the turbulent kinetic energy is 20% of its maximum value. The surface air temperature over the ice at $x = -50$ km is -9°C.

over the ice (Figure 7). This corresponds to the observed conditions at the location of the *Polar Circle* ($x = -15$ km) and the *Haakon Mosby* ($x = 100$ km). The wind vector below the low inversion over the ice has a small off-ice (positive x) component, while everywhere else the component is on-ice (not shown). This off-ice wind component over the ice prevented warm advection from destroying the shallow cold wedge at the surface. The converging low level air maintains a stationary frontal zone just iceward of the ice edge.

Wind stress. The dominant total wind stress feature is a positive spike just inside the ice edge (Figure 8). The pack ice τ_x values indicate a small off-ice forcing, whereas the open ocean forcing is on-ice. Gradients of τ_y, $\partial\tau_y/\partial x$, generate vertical motions in the upper ocean [e.g., *Pond and Pickard*, 1983]. A large $\partial\tau_y/\partial x$ occurs at the ice edge, associated with the roughness change, but an equally large $\partial\tau_y/\partial x$ of opposite sign occurs just iceward of the edge due to a change in wind speed, as in *Glendening*'s [1994] model. Note that the region of high wind stress (Figure 8) is

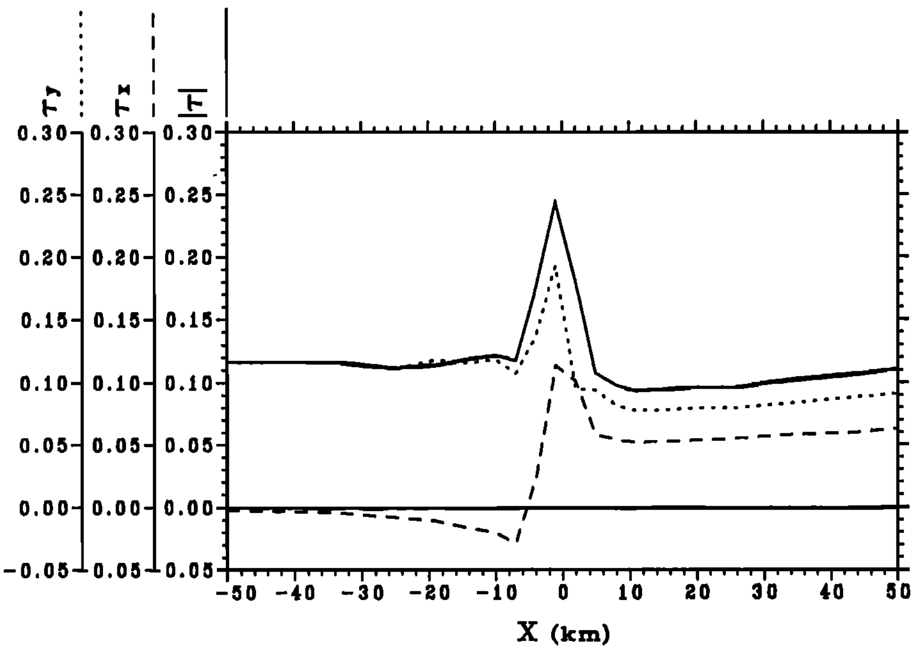

Figure 8. Model-predicted wind stress magnitude (solid line), negative x component of wind stress (dashed line) and negative y component (dotted line) for case study 1. The lower solid line indicates the zero value. Wind stress units are newtons per square meter.

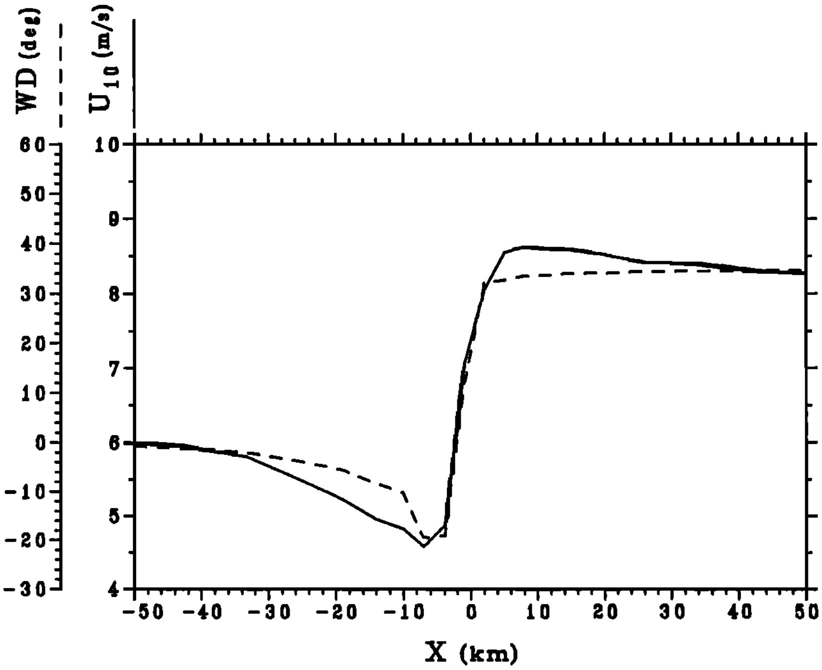

Figure 9. Model-predicted surface wind speed U_{10} (solid line) and relative surface wind direction WD, (dashed) for case study 1. The upper level geostrophic wind speed is 9 m s^{-1} magnitude at 35° relative direction.

narrower than the region of largest aerodynamic roughness (Figure 6). This occurs because the wind speed increases from 4.5 m s^{-1} for $x = -7$ km to 8.7 m s^{-1} for $x = 8$ km (Figure 9). The wind direction veers 50° across this region (Figure 9). The combined surface roughness and wind speed variations produce a wind stress curl reversal near the ice edge. Such a curl reversal could produce parallel bands of upwelling and downwelling in the ocean.

Factors Affecting Wind Stress

In this section we examine the role of factors B, W, S, and R in controlling wind stress variations for case study 1. The wind speed and direction changes noted above result from variations in factor B and factor W. The baroclinic effect (factor B) is relatively small because the strong changes in horizontal temperature differences over the ice are contained within a very shallow layer near the surface. Over the open ocean the ABL is deeper, but the temperature gradient is not large enough to make factor B significant.

In contrast, the wind speed reduction effect (factor W) increases by a factor of 4 across the ice edge. Far from the ice edge, factor W shows little variation. The rougher ice and small negative heat flux at the surface (5–10 W m^{-2}; see Figure 6) contribute to the small factor W over the ice. However, the primary influence is the presence of a shallow internal ABL. The internal ABL results from the contrast in temperature above the surface inversion, as maintained by advection of warm marine air, and the cold surface, as maintained primarily by radiational cooling. Downward turbulent heat flux into the surface initially create the internal ABL, but once formed, the internal ABL front continues to affect the wind stress even when the surface fluxes become small. The thermodynamics governing the interior ice ABL in this case study is analogous to the overall situation in the central Arctic, where warm advection above the ABL and more efficient radiational cooling of the surface than the air impose a stable thermal structure on the lower atmosphere [*Overland and Guest*, 1991]; this imposed background stability is often more important to wind stress than is the stability associated with surface heat fluxes [*Overland*, 1985; *Overland and Davidson*, 1992].

Although horizontal surface temperature gradients are large over the ice, heat fluxes are small because the surface wind is nearly parallel to the surface temperature gradients, the ABL is shallow, and the surface is well insulated by new snow. Therefore there is little effect of surface layer stability (factor S) upon wind stress (Figure 10). Over the ocean the surface temperature is constant (−1.7°C), but moderate upward surface fluxes (80 W m^{-2}) result from the recent over-ice history of the air parcels (Figure 4), and the relatively deep ABL prevents the air temperature from adjusting completely to the surface at the open ocean locations. These upward heat fluxes cause relatively little factor S enhancement of wind stress over the open ocean regions, the largest gradient occurring just inside the ice edge, where the surface temperature gradient is largest.

As discussed previously, large variations in surface roughness (factor R) occur in the MIZ region (Table 2; Figures 6 and 10). While the maximum variation of factor R is an order of magnitude greater than factor B or factor S effects, the factor R effects are of the same order as the factor W effects. Thus it would be incorrect to assume that the wind stress is proportional to factor R, even for small horizontal distances. Near the ice edge (-1 km $< x <$ 8 km), for example, the roughness effect decreases by a factor of 7 but the wind stress decreases by only a factor of 2.7. In the outer MIZ (-12 *km* $< x < -1$ km), roughness does not change significantly, but the wind stress changes by a factor of 2 owing to a reduction in wind speed. In the inner MIZ (−100

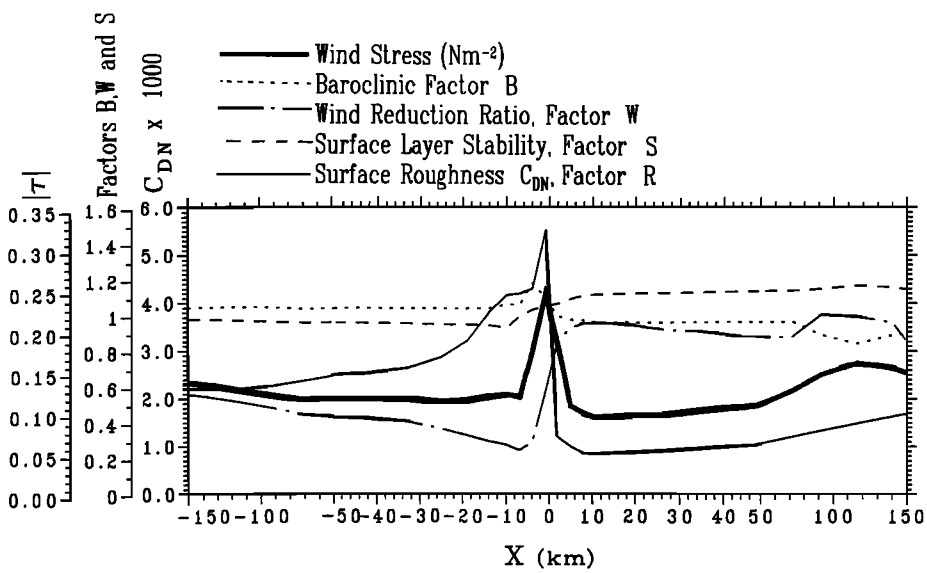

Figure 10. Model-predicted wind stress and factors B, W, S, and R for case study 1. The x scale is compressed by a factor of 3 for $x < -50$ km and $x > 50$ km.

km $< x < -11$ km) the roughness decreases, but the wind stress remains constant because the wind speed increases.

Which Creates the ABL Front: Surface Temperature or Roughness Gradients?

As a separate experiment the model is run with surface roughness constant (C_{DN} equals 1.5×10^{-3}) over the domain (results not shown). The resulting profiles of wind vector and temperature are qualitatively similar to the realistic case. An internal ABL again forms over the ice and the wind vector increases in magnitude and direction across the frontal region. This experiment indicates that for this case, the change of surface temperature is the dominant feature controlling the overall thermal and dynamic structure of the lower atmosphere across the MIZ. This does not mean that roughness is not important to wind stress; the wind stress in the constant roughness case is quite different from the realistic case. For example, the wind stress in the rough brash zone at the ice edge was a factor of 3 less for the constant roughness case than for the realistic roughness case. However, this case does demonstrate that the large changes in wind speed, associated with the change from the shallow ABL over the ice to the deep marine ABL, result primarily from temperature gradients, not from roughness gradients.

Summary of Case Study 1

For this case, surface roughness variations across the ice edge region (varying by a factor of 7) are greater than they are in previously referenced studies of MIZs. The minimum roughness occurs just seaward of the ice edge, where grease ice concentrations are highest. The maximum roughness occurs in a narrow (1 km) band of very rough rubble ice just inside the ice edge. Iceward of the narrow band of very rough ice, a 10-km-wide outer MIZ of rough, compact ice is about 5 times rougher than the grease ice region.

The low level air mass contrast resulting from converging surface winds nearly parallel to the ice edge creates a sharp, stationary ABL front just inside the ice edge. Changes in surface wind speed and direction across the ABL front greatly affect the wind stress field. The difference between the maximum and minimum wind stresses is a factor of 2.7, much less than the relative change in the roughness factor, as a result of compensating wind speed changes. The region of enhanced wind stress is concentrated in a region narrower than the region of rough MIZ ice, primarily owing to the presence of the ABL front. A significant wind stress curl reversal occurs near the ice edge. If grease ice had not been present, the wind stress over the ocean would have been about 50% higher and the relative importance of roughness variations would have been even smaller. Wind speed changes result primarily from surface thermal differences, not from surface roughness changes.

Case Study 2: Moderate Off-Ice Winds

Measurements

During off-ice wind conditions, sharp ABL fronts will not persist over an ice edge as occurs for case study 1. However, changes in ABL structure and surface heat fluxes across an MIZ still significantly affect the wind stress, as will be shown in the following case study.

The model simulates conditions on April 18, 1989 in the Fram Strait near the NW coast of Svalbard (Figure 11). During the CEAREX project, surface and upper air parameters are measured at the "O" camp and R/V *Polarbjoern* locations [*Lackmann et al.*, 1989; *Guest and Davidson*, 1989]. During the period 2300 April 17 to 0600 April 19, the *Polarbjoern* makes several transects within the MIZ region. Five upper air soundings are obtained at relative locations between $x = -5$ km and $x = 30$ km (Figure 12).

During this period the synoptic-scale geostrophic wind direction, GD_{top}, remains approximately constant from the north, or 315° relative to the SW-NE oriented ice edge. The magnitude of G_{top} gradually decreases from about 8.5 m s^{-1} to 5.5 m s^{-1}.

The first and last temperature profiles (represented by

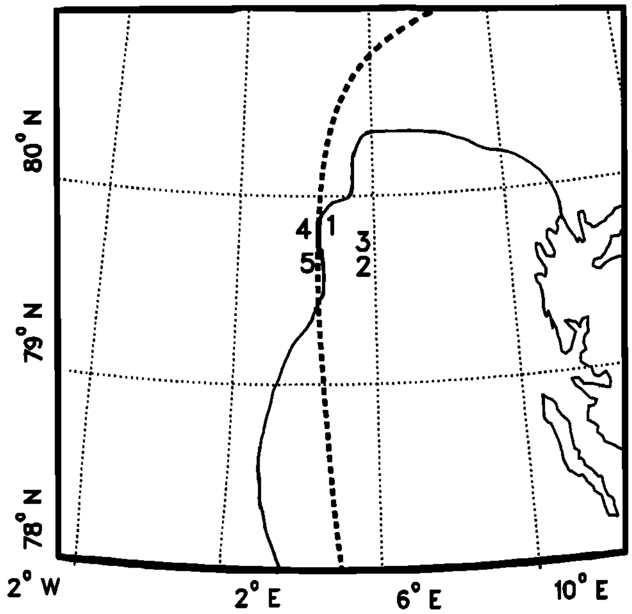

Figure 11. Map of case study 2 simulation showing the locations of R/V *Polarbjoern* during five rawinsonde soundings, numbered chronologically. The thick dashed line represents an air parcel trajectory above the boundary layer (north to south downwind). The model domain represents a section at right angles to the ice edge in the vicinity of the rawinsonde soundings.

solid and dotted lines in Figure 12), taken in roughly the same location, have a similar temperature structure despite the temporal separation of 31 hours and the decrease in G_{top}, so the xz cross section of potential temperature assumes thermal quasi-stationarity. The lower atmospheric structure at the "O" camp ($x = -120$ km) at 2309 UT, April 18, is characterized by a surface-based inversion extending to 200-m elevation, a slightly stable layer between 200 and 700 m, and another inversion layer between 700 and 900 m elevation (not shown). The temperature structure at the *Polarbjoern* location at $x = -5$ km at 2316 UT, April 18 is almost identical to the "O" camp sounding, except for the presence of a 170-m-thick well-mixed layer at the surface. The air mass over the MIZ at this time has previously been over an open ocean region south of Svalbard before moving to the north, moving cyclonically around the archipelago, then over the ice north of the *Polarbjoern* location, and finally moving south toward the MIZ (Figure 11). An upper level inversion is associated with a stratus cloud layer marking the top of the previous open ocean marine boundary layer. A new cold ABL forms in the lower 200 m as the air mass travels over ice and snow covered regions north and east of the MIZ region. This air mass is in approximate thermodynamic and dynamic equilibrium; surface turbulent fluxes are therefore small, and the temperature structure shows little horizontal variation in the region: $120 < x < -5$.

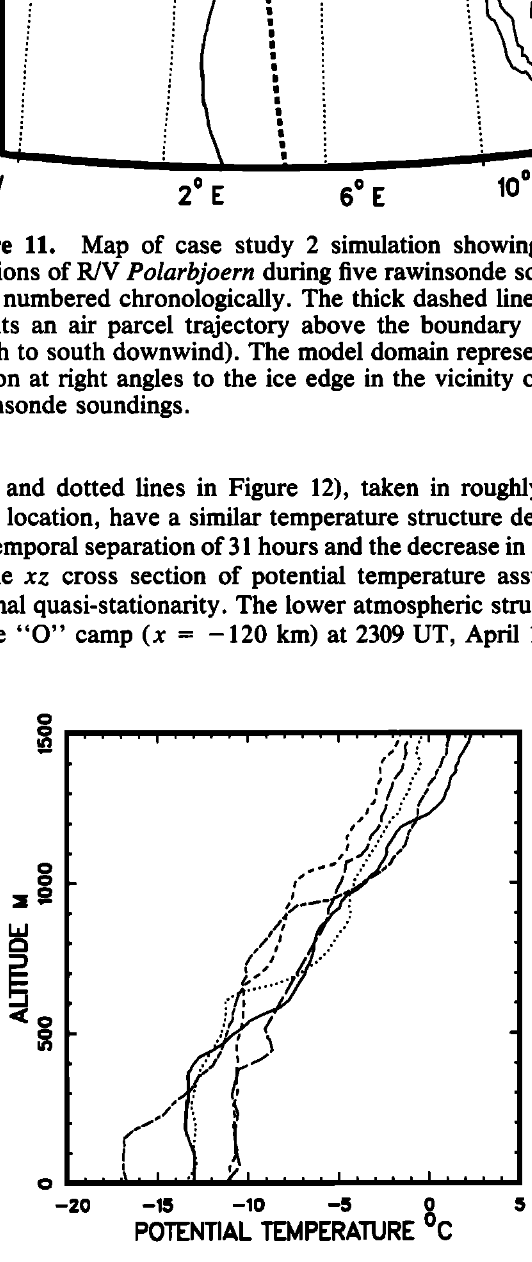

Figure 12. Profiles of potential temperature from the R/V *Polarbjoern* at times 2240 UT, April 17 (solid line); 0637 UT, April 18 (short-dashed line); 1029 UT, April 18 (long-dashed line); 2316 UT, April 18 (short- and long-dashed line); and 0621 UT, April 19, 1989 (dotted line). The relative locations x of these soundings are 6 km, 30 km, 23 km, −5 km, and 5 km. The absolute locations are shown in Figure 11.

Over the open ocean, however, dramatic changes in the ABL structure occur. The depth of the low level mixed layer, h, rises from 170 m to 700 m between $x = -5$ km and $x = 30$ km and the ABL potential temperature increases from −17.0°C to −10.5°C.

Model Initialization and Boundary Conditions

Domain. As for case study 1, the model represents a vertical slice perpendicular to the ice edge. G_{top} is kept constant at 6 m s^{-1} at a direction of 315° relative to the ice edge, matching the estimated forcing at 2300 UT, April 18. The potential temperature profile from the 2316 UT, April 18, rawinsonde sounding, at $x = -5$, specifies the initial, upwind, conditions for the model. This initial stratification profile represents the air mass between the MIZ and the "O" camp location.

Ice conditions. The surface roughness parameters z_0 and z_{0t} and the surface temperature T_0 are specified as before, except satellite visible images replace aircraft SAR images. Ice type and concentrations are estimated using advanced very high resolution radiometer (AVHRR) channel 2 data downloaded by the Norwegian Meteorological Institute in Tromsø and processed by R. Fett and associates at Naval Research Laboratory, Monterey, California. Although some cloudiness exists over the MIZ, a variable-concentration ice edge region, a small-floe inner MIZ region, and a large-floe pack ice region are distinguished on the 0919 UT April 19, AVHRR image. (On April 18 the entire MIZ is obscured by clouds.) This image and observations on board the *Polarb-*

Table 3. Surface Conditions for Case Study 2

Surface Type	x, km	Ice Concentration, %	$C_{DN} \times 1000$
Pack ice	<−100	>98	2.0–2.2
Inner MIZ	−100 to −20	98	2.2–3.4
Outer MIZ	−20 to −10	98–50	3.4–2.7
Diffuse ice edge region	−10 to 5	50–0	2.7–2.0
Open	>5	0	2.0–1.5

Unlike case study 1 (Table 2), there is no distinct ice edge; hence the extra column for ice concentration.

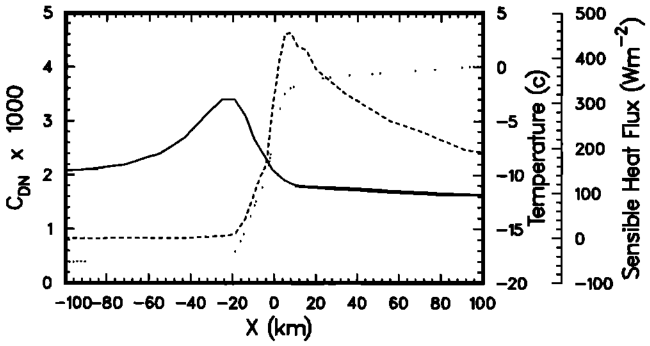

Figure 13. Surface boundary conditions for case study 2. The area-weighted average surface temperature (dotted line) and heat flux (dashed line) at the end of the model run and the neutral drag coefficient C_{DN} (solid line) throughout the run are shown as a function of distance from the ice edge, x.

joern determine the location of the ice edge and the boundary between the MIZ and the pack ice. An earlier image during very clear conditions at 0919, April 10, provides more detailed spatial information on the types and concentrations of sea ice which likely exist during the model period a week later.

The resulting surface types and C_{DN} estimates are given in Table 3 and Figure 13. The inner MIZ transitions between the relatively smooth compact pack ice and the rough, swell-affected, outer MIZ. C_{DN} is highest at high concentrations of rough ice. Unlike the previous case study, the ice edge is somewhat diffuse, so C_{DN} is lower at the ice edge than further into the ice. Grease ice is not observed, the ocean being too warm near the ice edge.

Surface temperature. The surface temperature T_{sfc} is again computed from net radiation, ice-snow thickness and conductivity, and turbulent fluxes (Figure 13). The downward longwave radiation, controlled by the stratus clouds, is assumed to be 240 W m^{-2} at all locations. Snow-ice thickness and conductivity specification are subjectively determined on the basis of ship observations, satellite images, and previous studies such as that of *Wettlaufer* [1991]. The internal ice temperature at the effective depth is $-16°$C over the pack ice and increases rapidly to $-1.7°$C in the inner MIZ (not shown). From the ice edge to x = 230 km, the ocean temperature increases from $-1.7°$C to 1.4°C. In regions with both ice and water, separate surface temperatures and heat fluxes are calculated for each surface, and an area-weighted average heat flux is determined for each surface grid point.

Results

Temperature structure. The model potential temperature field closely matches the observations (Figure 14). The air parcels have an off-ice component (left to right), advecting cold Arctic air over the warm ocean. The surface sensible heat flux is small over the ice and increases rapidly over the open water (Figure 13).

Wind stress. The maximum wind stress occurs just seaward of the ice edge, and unlike case study 1, the wind stress remains relatively high over the open ocean, being at least 2.5 times higher than the pack ice values (Figure 15). This is caused by a much greater wind speed over the open ocean compared with the pack ice (Figure 16). Due to the relatively constant wind direction (Figure 16), variations in τ_x and τ_y are similar (Figure 15).

Factors Affecting Wind Stress

For this case, factors B, W, S, and R all have a significant effect on the wind stress field (Figure 17). The factor B and S variations closely follow the surface heat flux variations, since the latter are largely responsible for both the horizontal temperature variations and the surface layer stability.

Variations in the wind speed reduction (factor W) are also similar to the surface heat flux variations but more pronounced than those for factors B or S (Figure 17). Values greater than unity indicate supergeostrophic wind velocities at an elevation of 10 m. These supergeostrophic wind velocities are caused, in part, by the acceleration of air parcels toward the low-pressure areas created by warming

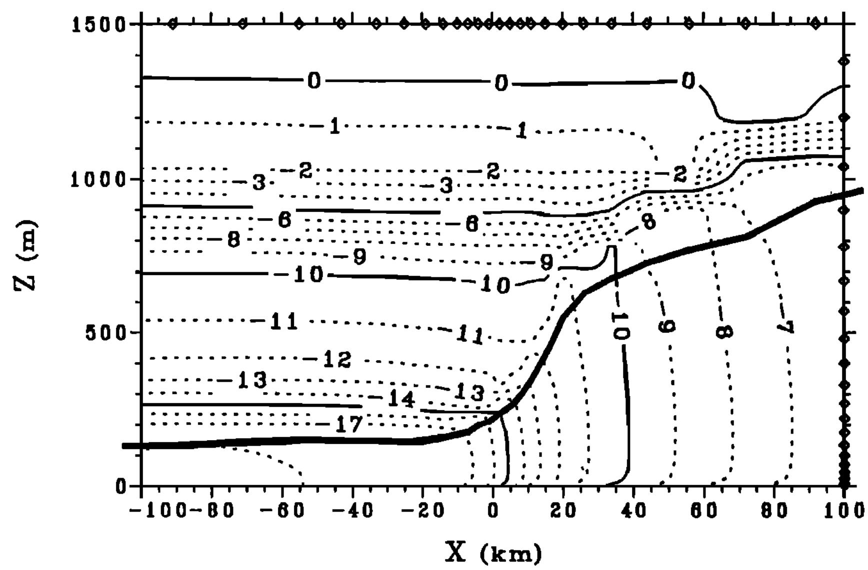

Figure 14. Isotherms of potential air temperature generated by the model simulation for case study 2. The solid thick line represents the top of the ABL, defined as in Figure 7.

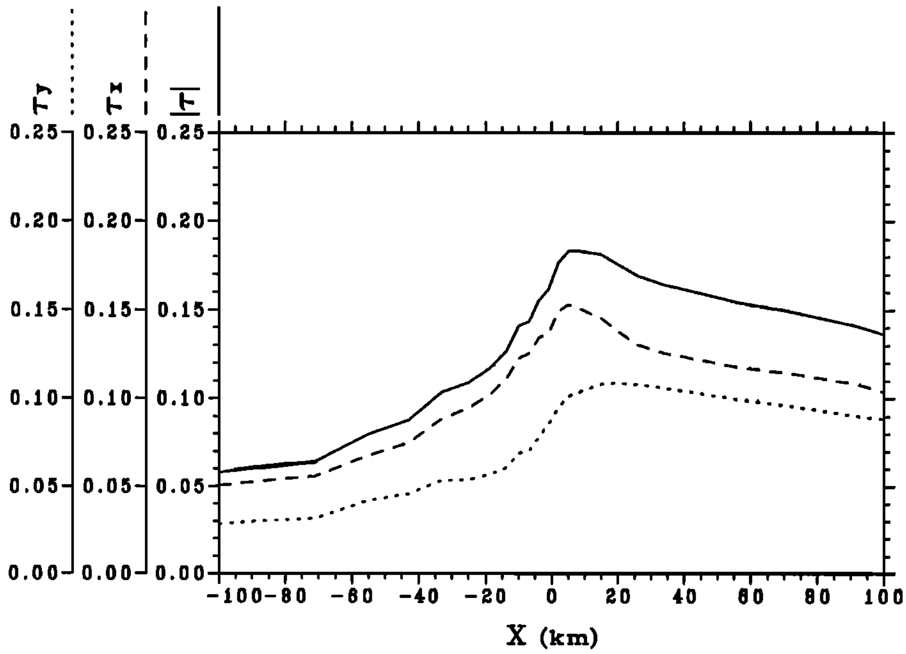

Figure 15. Model-predicted wind stress magnitude (solid line), negative x component of wind stress (dashed line) and negative y component (dotted line) for case study 2. Wind stress units are newtons per square meter.

over the ocean. This "ice breeze" addition to the wind vector is imbedded within the larger-magnitude background flow. Other factors contributing to the supergeostrophic winds over the open ocean are a lower surface roughness, a deeper and more unstable ABL, and nonlinear advection of momentum.

The surface roughness effect (factor R) is prescribed (Table 3; Figures 13 and 17). This effect dominates the wind stress field over the pack ice and the inner MIZ, where the surface heat flux is small. The maximum roughness effect occurs in the region of deformed and compact ice between the inner and outer MIZ, near $x = -20$ km. Between $x = -20$ km and $x = 5$ km, the roughness decreases to 60% of the maximum value, but the combination of factors B, W, and S more than counteracts this decrease, so the wind stress gradient increases. Over the open ocean, factor R variations are small and not important to wind stress variations.

Summary of Case Study 2

For this case study, the off-ice wind stress magnitude increases downwind across the ice edge, unlike the off-ice studies referenced previously [*Overland et al.*, 1983; *Reynolds*, 1984; *Kantha and Mellor*, 1989b; *Wefelmeier and Etling*, 1991], which experienced higher wind speeds (G_{top} = 13 m s^{-1}) than our case (G_{top} equals 6 m s^{-1}). At lower wind speeds, factors B, W, and S increase in importance relative to factor R effects. The lower wind speeds during our study are more typical of average conditions in the Fram Strait MIZ region, where wind speeds of 10 m s^{-1} or greater occur less than 10% of the time, according to our observations. The zone of roughness change is relatively diffuse, compared with case study 1, and the stress gradients are smaller.

The ratio of minimum to maximum values of factors B, W, S, and R are 1.35, 2.6, 1.3, and 2.3, respectively, indicating that factor W and factor R effects are the most important overall determinate of wind stress variations for case study 2, as they were for case 1. Factors B and S are correlated with each other, and with factor W, so that the combined effect of factors B, W, and S dominates the wind stress field in the ice edge region. These factors shift the position of maximum surface stress away from the position of maximum surface roughness.

A Simple Procedure for Specifying Wind Stress Within MIZs

Detailed understanding of the physics related to wind stress in MIZs requires the use of numerical ABL models. However, often a simpler approach is more practical. For example, theoretical studies of mesoscale oceanographic processes in MIZs may require a realistic wind stress field as an upper boundary condition. One approach is the use of Rossby number similarity theory [e.g., *Stull*, 1988; *Grant and Whiteford*, 1987], which assumes that the turning angle and wind stress are a function of surface layer stability, as parameterized by the Obukhov length scale L. *Brown* [1990] added further similarity functions to account for thermal wind and secondary circulations and applied the resulting model to MIZs. Brown's wind stress results were significantly closer to observations than were wind stress estimates based on constant surface wind speeds.

However, determining the Obukhov length scale L from the available observational data sets is often inaccurate as a result of uncertainties in the surface buoyancy flux. Another problem is that observations from sea ice regions show that the "external" stability, as represented by the overall static stability in the lower atmosphere, is also important to the surface wind stress vector, particularly when the ABL is shallow, which is common over sea ice [*Overland and Davidson*, 1992].

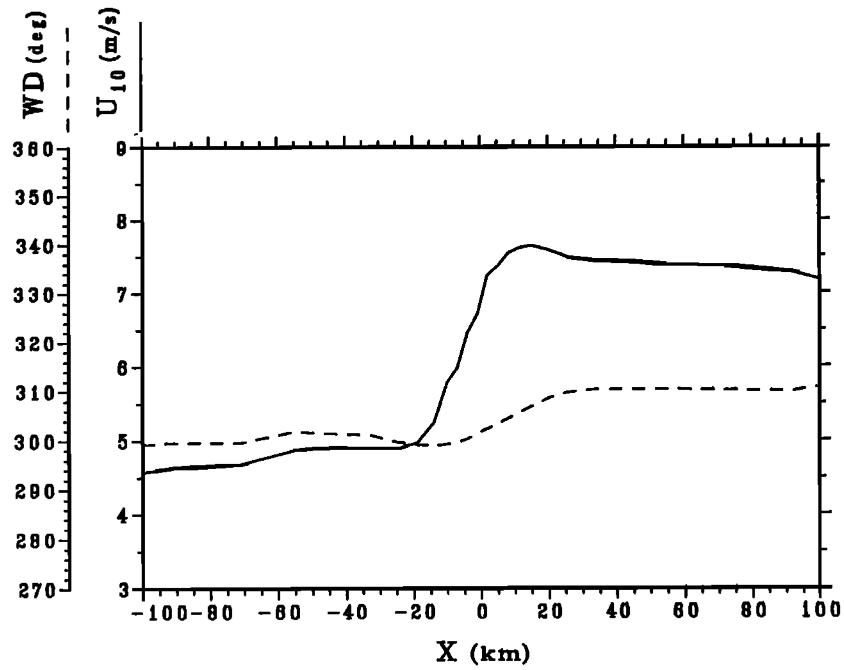

Figure 16. Model-predicted results of surface wind speed U_{10} (solid line) and relative surface wind direction WD (dashed line) for case study 2. The upper level geostrophic wind vector is 6 m s^{-1} magnitude at 315° relative direction.

A parameter which is influenced by external stability, surface layer stability and secondary circulations is the depth of the ABL, h. By using h, instead of L, as an ABL length scale, these effects are implicitly included. The following paragraphs describe a procedure which can be used to specify wind stress values which are generally consistent with measurements within or near MIZs. The procedure is most applicable for theoretical ice or ocean numerical modeling studies that require realistic but simple atmospheric forcing scenarios. Instead of assuming a constant surface wind vector, the approach is to assume a constant geostrophic wind vector and determine the surface wind vector based on a procedure that incorporates h and the surface roughness.

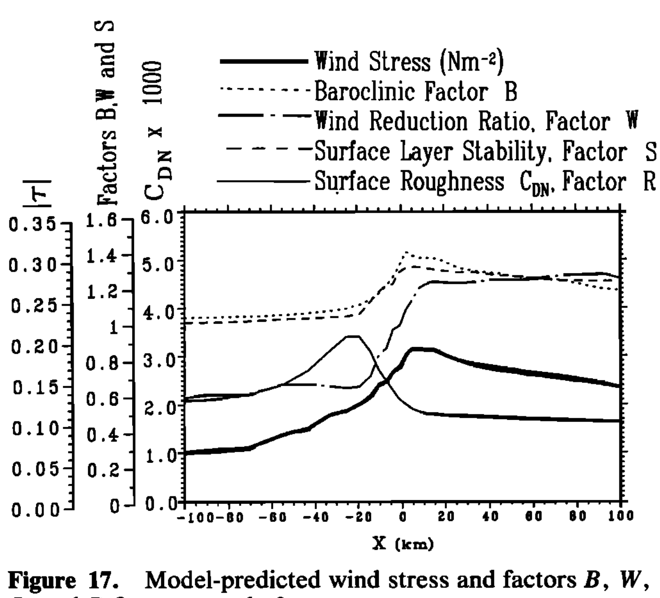

Figure 17. Model-predicted wind stress and factors B, W, S, and R for case study 2.

We will employ equations for factors W and W' that include the effects of G_{top}, C_D, and h in simplest form for a stationary, horizontally homogeneous boundary layer and then introduce empirical constants to account for effects not included in its derivation. We alter the expression derived by *Glendening* [1994] to obtain

$$W = \left\{\left(\left(\frac{C_1 C_D G_{sfc}}{fh}\right)^2 + \frac{1}{4}\right)^{1/2} + \frac{1}{2}\right\}^{-1} \tag{3}$$

$$W' = \tan^{-1}\left\{\left[\left(\left(\frac{C_2 C_D G_{sfc}}{fh}\right)^2 + \frac{1}{4}\right)^{1/2} - \frac{1}{2}\right]^{1/2}\right\} \tag{4}$$

where f is the Coriolis parameter and C_1 and C_2 are the empirical constants, which were unity in the original derivation. Here we set $C_1 = 2.5$ and $C_2 = 0.5$ to minimize the average difference between CEAREX observations [*Overland and Davidson*, 1992], and the predictions of (3) and (4). Using the tuned values of the coefficients with median observed G_{sfc}, C_D, and h variations across the MIZ produces changes in wind speed which match the median observed wind speed variations (Figure 2) quite well. In the observations, h was defined as the height of the base of the lowest inversion layer, with the inversion layer containing at least a 2.5°C increase in temperature. By tuning C_1 and C_2, we account for the average effect of the errors introduced by employing simplified equations under conditions where they are not strictly applicable, to retain the important effects of surface roughness and atmospheric stability on the slowing and turning of the wind vector near the surface.

Using (3) and (4) requires the specification of G_{sfc}, f, h, and C_D. Unless the three-dimensional thermal structure of the atmosphere is known, we suggest assuming G_{sfc} is constant and equal to G_{top} and that C_D is equal to C_{DN}. This is for simplicity and because some baroclinic and surface buoyancy effects are empirically included in the specifications of h and in the tuning of C_1 and C_2. Unless specific information is available, we suggest using values for C_{DN} and h that are based on typical values from observations. For example, Tables 1 and 2 provide values of C_{DN} that are applicable for compact or diffuse MIZ regions, respectively. Specifying the locations of the pack ice, the inner MIZ, the outer MIZ, the diffuse ice region, the pancake region, and other regions (required to estimate C_{DN}) for a particular study could use model output parameters such as ice concentration and thickness.

Generally, h values are not known for a particular case study. The authors and associates have used rawinsonde information from various projects to compile statistics concerning variations in h for different seasons in the Greenland Sea/Fram Strait MIZ. Based on this information, the following simple linear interpolation model can be used to specify an h field which is a valid for average conditions.

$$
\begin{array}{ll}
x \le x_{90} & h = h_{90} \\
x_{90} < x \le x_{50} & h = h_{90} + (x - x_{90}) \\
 & \quad \cdot (h_{50} - h_{90})/(x_{50} - x_{90}) \\
x_{50} < x \le x_{open} & h = h_{50} + (x - x_{50}) \\
 & \quad \cdot (h_{open} - h_{50})/(x_{open} - x_{50}) \\
x > x_{open} & h = h_{open}
\end{array}
\qquad (5)
$$

$h_{90} = 150$ m (all seasons)

$h_{50} = 300$ m (summer) $\quad h = 600$ m (nonsummer)

$h_{open} = 600$ m (summer) $\quad h = 1500$ m (nonsummer)

$x_{open} = 150$ km

The subscripts represent percentage ice concentration at the borders of four regions, a pack ice region (ice concentrations greater than 90%), two MIZ regions on both sides of an ice edge (defined as the 50% concentration line), and an open ocean region that exists farther than x_{open} from the ice edge.

A procedure for estimating wind stress in MIZs can now be outlined. First, specify the geostrophic wind vector and Coriolis parameter for the entire region. Second, determine the depth of the ABL, h, based on the locations of the pack ice–MIZ margin, x_{90}, and the ice edge, x_{50}, using (5). Next, use ice characteristics, such as concentration and thickness, to determine the areal-averaged surface drag coefficient C_D for each domain point. With this information, use (3) and (4) to predict factors W and W'. Finally, calculate the wind stress using (1), where for this simplified procedure factors B and S are set equal to 1 and factors B' and S' are set equal to zero. For many applications the geostrophic wind vector and the ABL depth can be considered constant in time; therefore the first two steps can be part of an initialization, while the rest of the procedure must be performed whenever ice conditions change.

Many caveats are inherent in the suggested method. The tuned coefficients C_1 and C_2 in (3) and (4) and the h values in equation (5) are based on average values in the Greenland Sea MIZ, for geostrophic wind speeds between 8 m s^{-1} and 15 m s^{-1}. Other regions and wind speeds may be different. In reality, h is a function of C_D and G_{sfc}. The approach is entirely one-dimensional, so that horizontal thermal effects, such as "ice breezes" and the relative wind direction effects are not explicitly modeled. For example, when the surface wind is parallel to the ice edge, the ABL depth and associated wind speed effects can change drastically over a distance of less than 10 km, as was seen in case study 1. Surface heat fluxes are also not explicitly included in the calculations but are included only implicitly through h variations. Many other physical processes are ignored. However, inclusion of these effects, many of which are highly nonlinear, cannot be accomplished with simple relationships. The goal here is to capture the first-order effects of atmospheric dynamic forcing variability in MIZs for average conditions without resorting to detailed atmospheric models.

Conclusions

We have demonstrated that wind stress in marginal ice zones depends upon a variety of factors in addition to surface roughness. These additional factors should be considered when realistic stress variations are required. In particular, the variation of wind speed often acts to counter that of surface roughness, so use of a constant wind speed overestimates stress changes due to surface roughness changes.

The surveyed observational and modeling results show that the surface wind speed in MIZs has considerable horizontal variability caused by the strong variations in surface and boundary layer conditions. Our numerical investigations, utilizing a detailed treatment of surface roughness and heat flux variations, illustrate the importance of these additional factors for two distinct cases. Case study 1 demonstrates the strong wind stress effects associated with an ABL front maintained by converging air near the ice edge. No such sharp front exists in case study 2; yet large surface heat flux differences create changes in ABL structure and dynamics which strongly affect the surface wind stress field. Both case studies show that a wind stress field based entirely on variations in surface roughness (i.e., assuming a constant surface wind speed and stability) can have large errors and can, for example, give the wrong sign for the wind stress curl.

While wind stress fields across an MIZ cannot be easily predicted for all combinations of conditions, some general conclusions can been made based on the examples provided by the ABL modeling and observational results presented here. Usually, the surface wind speed increases across the MIZ from pack ice to open ocean. The roughest surface generally occurs in the MIZ, with relatively smoother surfaces over the pack ice and open ocean regions. These persistent features create a wind stress maximum just iceward of the ice edge, with possibly another maximum farther out in the open ocean, and a stress minimum over the pack ice. Stress variations are generally smaller than roughness variations would suggest. This qualitative description of wind stress in MIZs and surrounding regions applies to most situations and can be used as a conceptual guideline for constructing realistic wind stress scenarios for use in ice and upper ocean studies.

Considering all the relevant effects on wind stress, as was done for the case studies presented here, requires the use of complex numerical ABL models. However, a relatively simple procedure can be used to estimate wind stress fields in the Greenland Sea–Fram Strait MIZ, region which are representative of many situations which are likely to occur. Use of procedures such as this to estimate surface stress, rather than assuming a constant surface wind speed as is the present norm, would improve the validity of ice and upper ocean dynamical models near the ice edge.

Acknowledgments. The support of the sponsors, the Naval Research Laboratory, Monterey, California (program element 0601153N), and the National Science Foundation (OPP-9316511), is gratefully acknowledged. The W.R. Church Computer Center at the Naval Postgraduate School provided computer time for the model runs. We thank the efforts of many individuals involved in our various field programs, who are too numerous to list.

References

Andreas, E. L, A theory for the scalar roughness and the scalar transfer coefficients over snow and sea ice, *Boundary Layer Meteorol.*, *38*, 159–184, 1987.

Andreas, E. L, W. B. Tucker III, and S. F. Ackley, Atmospheric boundary-layer modification, drag coefficient, and surface heat flux in the Antarctic marginal ice zone, *J. Geophys. Res.*, *89*, 649–661, 1984.

Bennett, T. J., and K. Hunkins, Atmospheric boundary layer modification in the marginal ice zone, *J. Geophys. Res.*, *91*, 13,033–13,044, 1986.

Brown, R. A., The planetary boundary layer in the marginal ice zone, in *MIZEX Bull. VII*, pp. 65–78, U.S. Army Cold Reg. Res. and Eng. Lab., Hanover, N. H., 1986.

Brown, R. A., Meteorology, in *Polar Oceanography, part A, Physical Science*, edited by W. O. Smith Jr., pp. 1–46, Academic, San Diego, Calif., 1990.

Chu, P. C., Ice breeze mechanism for an ice divergence-convergence criterion in the marginal ice zone, *J. Phys. Oceanogr.*, *17*, 1627–1632, 1987.

Fairall, C. W., and R. Markson, Mesoscale variations in surface stress, heat fluxes, and the drag coefficient during the 1983 Marginal Ice Zone Experiment, *J. Geophys. Res.*, *92*, 6921–6932, 1987.

Glendening, J., Dependence of boundary layer structure near an ice-edge coastal front upon geostrophic wind direction, *J. Geophys. Res.*, *99*, 5569–5581, 1994.

Grant, A. L. M., and R. Whiteford, Aircraft estimates of the geostrophic drag coefficient and the Rossby similarity function A and B over the sea, *Boundary Layer Meteorol.*, *39*, 219–231, 1987.

Guest, P. G., A numerical, analytical and observational study of the effect of clouds on wind stress during the central Arctic winter, Ph.D. dissertation, 187 pp., Nav. Postgrad. Sch., Monterey, Calif., 1992.

Guest, P. S., and K. L. Davidson, The effect of observed ice conditions on the drag coefficient in the summer East Greenland Sea marginal ice zone, *J. Geophys. Res.*, *92*, 6943–6954, 1987.

Guest, P. S., and K. L. Davidson, CEAREX/"O" and "A" camp meteorology atlas, *Rep. NPS-63-89-007*, 70 pp., Nav. Postgrad. Sch., Monterey, Calif., Sept. 1989.

Guest, P. S., and K. L. Davidson, The aerodynamic roughness of different types of sea ice, *J. Geophys. Res.*, *96*, 4709–4721, 1991.

Guest, P. S., and K. L. Davidson, A study of the factors controlling the value of the surface temperature of sea ice, paper presented at Third Conference on Polar Meteorology and Oceanography, Am. Meteorol. Soc., Portland, Oreg., Sept. 29 to Oct. 2, 1992.

Guest, P. S., K. L. Davidson, J. E. Overland, and P. A. Frederickson, Atmosphere-ocean interactions in the marginal ice zones of the Nordic seas, in *Arctic Oceanography: Marginal Ice Zones and Continental Shelves*, *Coastal Estuarine Stud.*, vol. 49, edited by W. O. Smith and J. M. Grebeier, AGU, Washington, D. C., in press, 1995.

Häkkinen, S., Coupled ice-ocean dynamics in the marginal ice zones: Upwelling/downwelling and eddy generation, *J. Geophys. Res.*, *91*, 819–832, 1986a.

Häkkinen, S., Ice banding as a response of the coupled ice-ocean system to temporally varying winds, *J. Geophys. Res.*, *91*, 5047–5053, 1986b.

Häkkinen, S., A coupled dynamic-thermodynamic model of an ice-ocean system in the marginal ice zone, *J. Geophys. Res.*, *92*, 9469–9478, 1987.

Häkkinen, S., G. L. Mellor, and L. H. Kantha, Modeling deep convection in the Greenland Sea, *J. Geophys. Res.*, *97*, 5389–5408, 1992.

Holton, J. R., *An Introduction to Dynamic Meteorology*, 331 pp., Academic, San Diego, Calif., 1972.

Ikeda, M., Wind-induced mesoscale features in a coupled ice-ocean system, *J. Geophys. Res.*, *96*, 4623–4629, 1991.

Johannessen, O. M., J. A. Johannessen, S. Sandven, and K. L. Davidson, Preliminary results of the Marginal Ice Zone Experiment (MIZEX) summary operations, in *The Environment of the Nordic Seas*, edited by B. H. Hardle, pp. 665–679, Springer-Verlag, New York, 1985.

Kantha, L. H., and G. L. Mellor, A two-dimensional coupled ice-ocean model of the Bering Sea marginal ice zone, *J. Geophys. Res.*, *94*, 10,921–10,935, 1989a.

Kantha, L. H., and G. L. Mellor, A numerical model of the atmospheric boundary layer over a marginal ice zone, *J. Geophys. Res.*, *94*, 4959–4970, 1989b.

Kellner, G., C. Wamser, and R. A. Brown, An observation of the planetary boundary layer in the marginal ice zone, *J. Geophys. Res.*, *92*, 6955–6965, 1987.

Lackmann, G. M., P. S. Guest, K. L. Davidson, R. J. Lind, and J. Gonzalez, CEAREX/*Polarbjoern* meteorology atlas, *Rep. NPS-63-89-005*, 550 pp., Nav. Postgrad. Sch., Monterey, Calif., Sept. 1989.

Leppäranta, M., and W. D. Hibler, The role of plastic ice interaction in marginal ice zone dynamics, *J. Geophys. Res.*, *90*, 11,899–11,909, 1985.

Lindsay, R. W., and A. L. Comiskey, Surface and upper-air observations in the eastern Bering Sea, February and March, 1981, *Tech. Memo. ERL-PMEL-35*, 90 pp., Natl. Oceanic and Atmos. Admin., Washington, D.C., 1982.

Maykut, G. A., Large-scale heat exchange and ice production in the central Arctic, *J. Geophys. Res.*, *87*, 7971–7984, 1982.

McPhee, M. G., G. A. Maykut, and J. H. Morison, Dynamics and thermodynamics of the ice/upper ocean system in the marginal ice zone of the Greenland Sea, *J. Geophys. Res.*, *92*, 7016–7031, 1987.

Overland, J. E., Atmospheric boundary layer structure and drag coefficients over sea ice, *J. Geophys. Res.*, *90*, 9029–9049, 1985.

Overland, J. E., and K. L. Davidson, Geostrophic drag coefficients over sea ice, *Tellus*, *Ser. A*, *44*, 54–66, 1992.

Overland, J. E., and P. S. Guest, The Arctic snow and air temperature budget over sea ice during winter, *J. Geophys. Res.*, *96*, 4651–4662, 1991.

Overland, J. E., M. Reynolds, and C. Pease, A model of the atmospheric planetary boundary layer over the marginal ice zone, *J. Geophys. Res.*, *88*, 2836–2840, 1983.

Parkinson, C. A., and W. M. Washington, A large-scale model of sea ice, *J. Geophys. Res.*, *84*, 311–337, 1979.

Pond, S., and G. L. Pickard, *Introductory Dynamical Oceanography*, 2nd ed., 349 pp., Pergamon, New York, 1983.

Reynolds, M., On the local meteorology at the marginal ice zone of the Bering Sea, *J. Geophys. Res.*, *89*, 6515–6524, 1984.

Røed, L., Sensitivity studies with a coupled ice-ocean model of the marginal ice zone, *J. Geophys. Res.*, *88*, 6039–6042, 1983.

Røed, L., A thermodynamic coupled ice-ocean model of the marginal ice zone, *J. Phys. Oceanogr.*, *14*, 1921–1929, 1984.

Røed, L., and J. O'Brien, A coupled ice-ocean model of upwelling in the marginal ice zone, *J. Geophys. Res.*, *88*, 2863–2872, 1983.

Shaw, W. J., R. L. Pauley, T. M. Gobel, and L. F. Radke, A case study of atmospheric boundary layer mean structure for flow parallel to the ice edge: Aircraft observations from CEAREX, *J. Geophys. Res.*, *96*, 4691–4708, 1991.

Smedstad, O. M., and L. P. Røed, A coupled ice-ocean model of ice break-up and banding in the marginal ice zone, *J. Geophys. Res.*, *90*, 876–882, 1985.

Smith, D. C., IV, A. A. Bird, and W. P. Budgell, A numerical study of mesoscale ocean eddy interaction with a marginal ice zone, *J. Geophys. Res.*, *93*, 12,461–12,473, 1988.

Smith, S. D., Coefficients of sea surface wind stress, heat flux, and wind profiles as a function of wind speed and temperature, *J. Geophys. Res.*, *93*, 15,467–15,472, 1988.

Stull, R. B., *An Introduction to Boundary Layer Meteorology*, 680 pp., Kluwer Academic, Norwell, Mass., 1988.

Walter, B., and J. E. Overland, Aircraft observations of the mean and turbulent structure of the atmospheric boundary layer during spring in the central Arctic, *J. Geophys. Res.*, *96*, 4663–4673, 1991.

Walter, B., J. Overland, and R. Gilmer, Air-ice drag coefficients for first-year sea ice derived from aircraft measurements, *J. Geophys. Res.*, *89*, 3550–3560, 1984.

Wefelmeier, C., and D. Etling, The influence of sea ice distribution on the atmospheric boundary layer, *Z. Meteorol.*, *41*, 333–342, 1991.

Wettlaufer, J. S., Heat flux at the ice-ocean interface, *J. Geophys. Res.*, *96*, 7215–7236, 1991.

K. L. Davidson and P. S. Guest, Department of Meteorology, Naval Postgraduate School, 589 Dyer Road, Monterey, CA 93943-5114. (e-mail: davidson@nps.navy.mil; pguest@nps.navy.mil)

J. W. Glendening, Marine Meteorology Division, Naval Research Laboratory, Monterey, CA 93943.

(Received June 14, 1993; revised December 20, 1994; accepted December 27, 1994.)